Physica Medica 141 (2026) 105708

Contents lists available at ScienceDirect

Physica Medica

journal homepage: www.elsevier.com/locate/ejmp

Original paper

Monte Carlo simulation of a cabinet kilovoltage X-ray irradiator

E. Theodoridou [a,b,i,1], R. Dong [a,c,1], C.C. King [a,d,*,1], G. Poludniowski [e,f], P. Häring [g,h], E. Hain [a,i], C. Litou [a,j], E. Voutou [a,j], P. Foka [k,l], N. Sammut [b], J. Seco [a,i,2,**], M.F. Spadea [d,2]

[a] Division of Biomedical Physics in Radiation Oncology, German Cancer Research Center (DKFZ), Im Neuenheimer Feld 280, Heidelberg, 69120, Germany
[b] Faculty of Information & Communication Technology, L-Università ta' Malta, Msida MSD 2080, Malta
[c] School of Physics, Southeast University, No. 2 Southeast University Road, Nanjing, 210094, China
[d] Institute of Biomedical Engineering, Karlsruhe Institute of Technology (KIT), Fritz-Haber-Weg 1, Karlsruhe, 76131, Germany
[e] Department of Clinical Science, Intervention and Technology (CLINTEC), Karolinska Institutet, ANA Futura, Alfred Nobels Allé 8, Huddinge, SE-141 52, Sweden
[f] Department of Nuclear Medicine and Medical Physics, Karolinska University Hospital, D1:00, Framstegsgatan 21, Solna, 171 64, Sweden
[g] Heidelberg Institute for Radiation Oncology (HIRO), National Center for Radiation Research in Oncology, Heidelberg, 69120, Germany
[h] Division of Medical Physics in Radiation Oncology, German Cancer Research Center (DKFZ), Im Neuenheimer Feld 280, Heidelberg, 69120, Germany
[i] Department of Physics and Astronomy, Heidelberg University, Im Neuenheimer Feld 226, Heidelberg, 69120, Germany
[j] Department of Physics, Aristotle University of Thessaloniki, University Campus, Thessaloniki, 54124, Greece
[k] GSI Helmholtzzentrum für Schwerionenforschung GmbH, Planckstraße 1, Darmstadt, 64291, Germany
[l] European Organization for Nuclear Research (CERN), 1211 Geneva 23, Switzerland

ARTICLE INFO

Keywords:
Monte Carlo simulation
Kilovoltage X-ray irradiator
Dosimetry
Half-value layer (HVL)

ABSTRACT

Introduction: We present a rigorously defined dosimetric Monte Carlo (MC) model of the MultiRad225 kilovoltage X-ray irradiator, which is validated using experimental techniques. Previous MC studies performed with the MultiRad225 lacked rigorous dosimetric validation.
Methods: Experimental measurements are conducted with an ionization chamber and radiochromic film with beam energies of 119, 160, and 200 kV. MC simulations are conducted mimicking each experiment. Both beam quality (half-value layer, HVL) and quantity (dose rate) are assessed with these methods.
Results: MC simulated dose rates and HVL values show close agreement with experimental results across varying source-to-surface distances (SSD) for each beam energy with most dose rate simulations falling within 5% of the experimentally measured values.
Conclusions: This work provides a validated MC model as a foundation for future studies with the MultiRad225. The MC model utilizes a comprehensive geometry which accurately captures relevant physical phenomena.

1. Introduction

Radiation therapy (RT) is a cornerstone of cancer treatment, with more than half of all patients receiving RT and approximately 40% achieving curative outcomes [1]. However, the dose-dependent nature of RT is a significant clinical challenge, as increasing tumor control probability (TCP) is often accompanied by a rise in normal tissue complication probability (NTCP), limiting the therapeutic window [2]. Because of this, it is vitally important to utilize precise dosimetry techniques both in the clinic, and experimentally [2,3]. X-ray radiotherapy (XRT) is the most commonly used RT modalities due to its cost-effectiveness and ease of implementation. While other modalities may offer advantages in tailoring treatments for specific tumors, XRT still remains important in many cases or may be used in combination with other techniques [3–6].

With the constantly evolving XRT technology, it is becoming increasingly difficult to establish precise dosimetry techniques [7]. Thus, Monte Carlo (MC) simulations are often used in conjunction with experimental dosimetry. However, MC requires rigorously characterized geometries and physics models, requiring careful consideration of all simulation inputs [8–10].

* Corresponding author.
** Correspondence to: DKFZ, Im Neuenheimer Feld 280, 69120, Heidelberg, Germany
E-mail addresses: ccking9295@gmail.com (C.C. King), j.seco@dkfz-heidelberg.de (J. Seco).
[1] E Theodoridou, R Dong, and CC King contributed equally to this work.
[2] Joint last author.

https://doi.org/10.1016/j.ejmp.2025.105708
Received 31 July 2025; Received in revised form 25 October 2025; Accepted 12 December 2025
Available online 22 December 2025

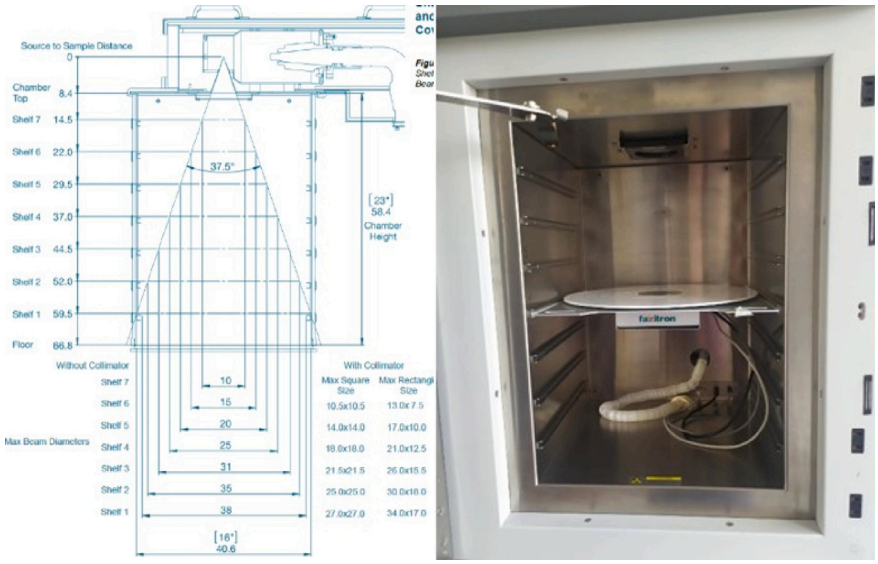

Fig. 1. Schematic diagram (left) and irradiation chamber image (right) of MultiRad225 system from Precision. Sample placement shelf, as shown in image, is in the 4th position with an initial SSD of 37.0 cm (before accounting for sample/dosimeter height, phantom, etc.).

In this study, we perform a comprehensive experimental characterization of a kilovoltage X-ray irradiator using ionization chamber and radiochromic film dosimetry. To complement our measurements, we develop an MC model to simulate dosimetric parameters across different beam configurations. This integrated approach serves to validate our experimental framework and establish a modeling foundation for future studies.

All measurements presented here are performed using the MultiRad225 from Precision X-ray, shown in Fig. 1. The MultiRad225 is an easily accessible commercial X-ray irradiator capable of generating X-rays with energies up to 225 kV and can reach a beam current of up to 30 mA. The irradiators in the MultiRad family (160, 225, 350) are primarily designed for biological samples such as cell cultures and small animals [11]. Thus, these systems are frequently employed in experimental XRT and radiobiology studies [12–14] as well as experiments with different X-ray modalities [15,16]

Previous similar studies include MC studies on other orthovoltage irradiators such as the Pantak SXT 150 [17], Philips RT-250 [18], and a Hitachi MBR-320 [19]. While MC studies have also been done on the MultiRad225, they lacked rigorous dosimetric validation [20,21]. In [22], another similar study has reported FLASH dose rates exceeding 100 Gy/s using Comet MXR-160/22 and MXR-165 X-ray tubes. Here, we believe, the MC model used to calculate this dose rate was only partially validated with dosimetric measurements.

2. Methods

The X-ray tube contained within the MultiRad225 system has an inherent filtration from 2 mm Be. For the results presented here, we additionally use a 0.5 mm Cu filter unless indicated otherwise. The machine also includes a removable shelf which can be fixed at various source-to-surface distances (SSD) ranging from 14.5 cm to 59.5 cm at 7.5 cm increments, as shown in Fig. 1. At an SSD of 37 cm, the field size of the X-ray beam is 25 × 25 cm. Experiments are performed at 119 kV, 160 kV, and 200 kV with the beam current adjusted to maintain constant beam power.

2.1. Half-value layer measurement for beam quality

Half-value layer (HVL) measurements are conducted to evaluate X-ray beam quality and energy distribution by measuring the ability of the beam to penetrate materials. As shown in Fig. 2, a large tungsten collimator with a 2.5 cm opening is placed at the top of the machine. Experiments are performed with a PTW TM30013 Farmer ionization chamber [23] at 119 kV, 160 kV, and 200 kV using Al (0.5 mm) and Cu (0.1 mm) plates and a 0.25 mm Cu filter instead of the 0.5 mm Cu filter mentioned previously. The beam was incrementally attenuated by stacking the plates, one at a time, on top of each other in the path of the beam, directly below the collimator. The Farmer chamber is suspended at an SSD of 44.5 cm, which is the distance from the source which maintains a sufficient separation from the interior surfaces.

The HVL values are derived by interpolating the attenuator thickness where the dose dropped to half (HVL1) or one quarter (HVL2) of its initial value. Dose measurements are performed with varying attenuator thickness for each combination of energy and attenuator material. HVL experiments are also simulated using the EGSnrc [24] and SpekPy [25] software packages. Using SpekPy (version 2.0.13.1) with the kqp physics model [26,27] and NIST linear attenuation coefficients [25], HVL is calculated in a similar method to the experiment, iteratively increasing the attenuation of the beam. SpekPy also includes a native HVL function for calculating HVL directly. This function was not used and is further discussed in Appendix. The EGSnrc Monte Carlo software package is described in further detail in Section 2.4.

2.2. Dose rate measurement for beam quantity

X-ray dosimetry is performed using the TM23343 Markus ionization chamber from PTW [23] and the EBT-XD Gafchromic film. The choice of the detector and film is based on reducing the effect of the detector on the measurement (i.e. from the ion chamber entrance window). The film is placed on top of a 1 cm thick RW3 (water equivalent material) plate while the Markus chamber is placed in a cavity located between two RW3 plates with the entrance window unobstructed. Both are placed in the center of the beam. The ionization was cross calibrated according to the dose to water calibration factors provided by PTW.

The Markus chamber is connected to a PTW Unidos electrometer and a potential of 300 V is applied to the chamber. The chamber is irradiated for 360 s and the charge collected by the chamber is recorded and corrections are made for air temperature and pressure, as well as inverse polarity, according to the TRS-398 guidelines [28]. The measured dose is calculated from the charge collected by the chamber. Films are pre-scanned and rescanned 24 h after cutting and irradiating, respectively. The films are exposed for 360 s, and dose calculations follow pixel intensity differences. Scanning is performed using an Epson

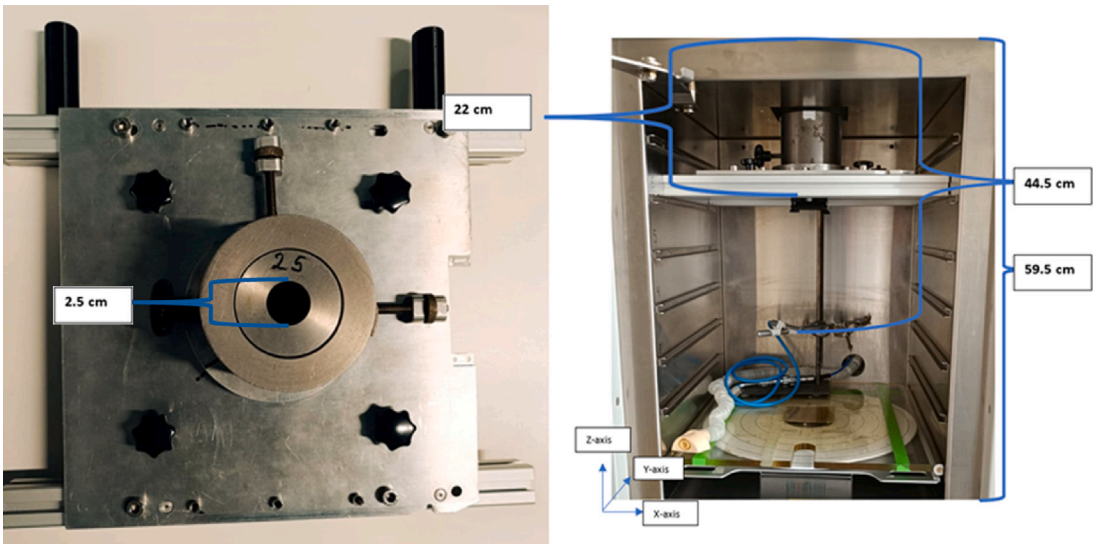

Fig. 2. Image of tungsten collimator (left) with 2.5 cm opening used in HVL measurements. The collimator is placed at the top of the irradiation chamber as shown (right).

10000XL scanner and the difference in optical density between the films before and after irradiation is converted to dose delivered using the method outlined in [29].

2.3. Dosimetry and calibration

The Semiflex 0.125 cm^3 chamber was utilized for cross-calibration and was calibrated by the PTW Calibration Lab for the beam qualities TH200, TH140, and TH100. The corresponding HVL values were obtained from the calibration certificate and plotted against the k_Q factors. For HVL values measured in this study that fell between the established calibrated points, the k_Q factors were determined by means of interpolation. These interpolated k_Q factors were subsequently employed to determine the final dose for the Markus chamber, as shown in Fig. 3. This procedure aligns with the recommended method for determining k_Q factors outlined in TRS-398 [28], Section 9.2.1, thereby ensuring the accuracy of dose measurements.

Radiochromic films were calibrated using a reference 200 kV X-ray beam (HVL = 0.74 mm Cu), which is representative of the experimental beam quality. A series of known doses were administered to the films, and optical densities (ODs) were subsequently measured using the red channel of the scanner. A dose–response curve was generated by fitting OD versus dose using a polynomial function [30]. It should be noted that no correction for energy dependence was applied. Ashland (2021) reports minimal energy response of EBT-XD films across the kV range used. The upper limit of the estimated uncertainty, attributable to film response, scanner variability, and film uniformity, has been ascertained to be approximately five percent [31].

It is important to note that the dosimeters employed in this study: the PTW Farmer chamber, Advanced Markus parallel-plate chamber, and EBT-XD radiochromic films, exhibit varying degrees of energy dependence within the kilovoltage range. The Farmer chamber has been observed to demonstrate a slight overresponse at low energies [32], while the Markus chamber has been shown to exhibit an energy-dependent response in the kilovoltage range, which could potentially account for discrepancies in output factor measurements [33]. EBT-XD films, which have been developed for high-dose applications, exhibit minimal energy dependence (less than 5%) from 100 keV to 18 MeV [34]. Calibration was performed under conditions that closely matched the experimental setup; nevertheless, these small energy-dependent effects may partially explain the minor differences observed between Monte Carlo simulations and measurements, particularly in regions affected by beam hardening.

2.4. Monte Carlo simulation

The X-ray tube is modeled using the EGSnrc/BEAMnrc Monte Carlo code based on the tube parameters outlined in Table 1. To get statistically significant results, simulations are conducted with 10^9 incident electrons. These electrons are directed at a tungsten anode target. The full geometry for the model is shown in Fig. 4. Simulations are performed using kinetic energies of 200 keV, 160 keV, and 119 keV, matching the experimental measurements.

To enhance computational efficiency, Bremsstrahlung directional splitting is employed with a splitting factor of 200. For all simulations, the kinetic energy cutoffs are set to 512 keV for electrons and 1 keV for photons. Additionally, low-energy physical processes — including atomic relaxation, electron impact ionization, and Rayleigh scattering — were explicitly included to improve the accuracy of the simulations. Electron impact ionization is simulated using penelope cross sections.

The MC simulation outputs a phase-space file containing the characteristics of particles crossing a scoring plane within the film and Markus chamber geometries. The phase-space file is then analyzed by Beamdp (part of EGSnrc software package) in order to get the spectral fluence. Within the Beamdp interface, an annular region centered at the z-axis is used with a maximum radius matching the sensitive volume of the ionization chamber or analyzed region of interest of the radiochromic films. The output is set as a point graph of estimated real fluence.

The upstream X-ray tube assembly and filtration system are explicitly modeled in order to account for scattering effects, including a 0.2 cm beryllium window, a 1.0 cm tungsten target, a 1.63 cm lead shield, a front and back collimator of 2.45 cm and 3.15 cm, respectively, followed by a 4.73 cm air gap, a 0.229 cm stainless steel plate, and a 0.05 cm copper filter. This configuration reproduces the beam-hardening and filtration conditions of the experimental setup. All materials are defined using standard compositions and densities from the BEAMnrc material library.

Ionization chamber geometry and materials. The Markus plane-parallel ionization chamber is modeled in BEAMnrc based on the manufacturer's specifications and positioned at an SSD of 12.6 cm, as shown in Fig. 4. The Markus chamber itself consists of a 0.03 cm polyethylene entrance window, a 0.127 cm air cavity, and a 1.22 cm RW3 backscatter layer. The chamber axis is aligned coaxially with the beam, and the dose to air in the sensitive volume is scored to obtain the chamber response. All geometric and material parameters were referenced from the manufacturer's technical data (Precision, USA).

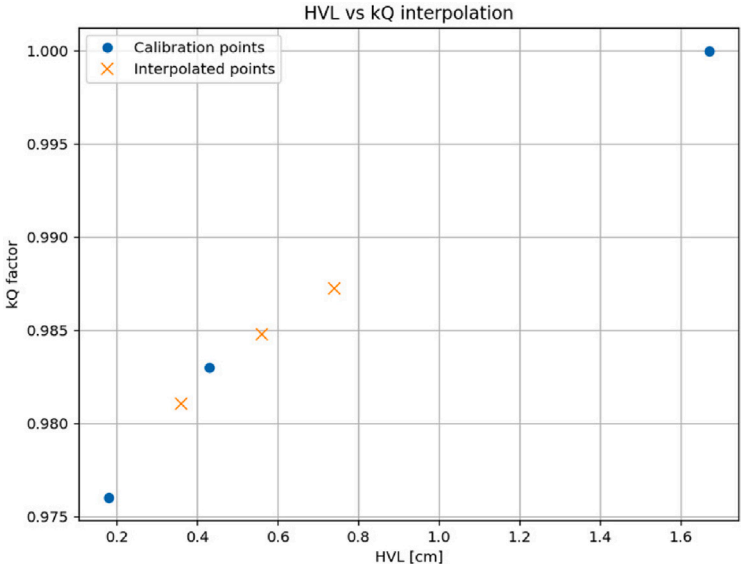

Fig. 3. The figure illustrates calibration and interpolated kQ values for copper HVLs. Dots represent the PTW calibration points with known kQ factors, while the crosses indicate the kQ values interpolated for the copper HVLs measured in this work. The interpolation process was executed in accordance with the TRS-398 formalism [28], as delineated in Section 9.2.1, to determine the absorbed dose using the Markus chamber.

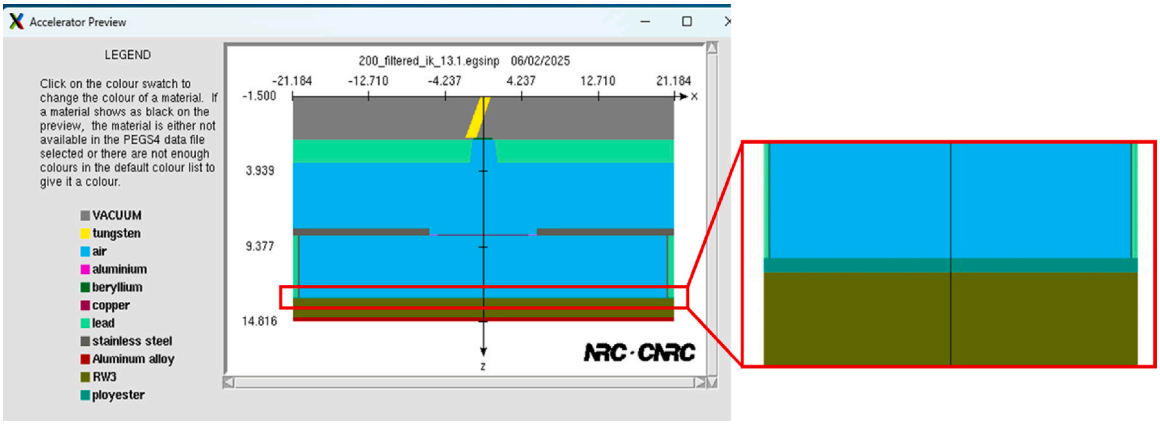

Fig. 4. Image of X-ray irradiator and radiochromic film geometry used in MC simulations. Scoring plane (not shown) is placed in the center of the polyester layer (center layer of zoomed-in image).

Radiochromic film geometry and materials. The radiochromic film assembly includes a 0.0125 cm polyester encapsulation layer, a 1.4 cm RW3 solid-water backing, and a 0.285 cm aluminum alloy base. The active dosimetric layer is placed in the middle of the polyester encapsulation, and the entire film assembly is positioned 13.1 cm from the X-ray source, perpendicular to the beam axis. Dose is scored within the active layer region and averaged over the same area corresponding to the optical film readout used in the experimental analysis. All structural and material parameters of the film and encapsulation were obtained from the manufacturer's technical documentation (Precision, USA).

Table 1
Relevant irradiator specific parameters used in MC model.

Parameter	Value
Total tube power [kW]	3.56
Beam energy [kV]	200,160,119
Beam current [mA]	17.8,22.3,30
Anode angle [°]	30
Entrance window [mm Be]	2
*Additional filtration [mm Cu]	0.5

Note: Cu filtration value here is for beam quantity simulations.

2.5. Monte Carlo air kerma and dose rate calculation

Air kerma is the energy transferred to charged particles per unit mass from indirectly ionizing radiation. We calculate air kerma rate using the fluence spectrum from the MC simulation with

$$K\left[\frac{\text{MeV}}{\text{g particle}}\right] = \sum_i \Phi_i \left[\frac{1}{\text{cm}^2\ \text{MeV particle}}\right] \times E_i[\text{MeV}]\Delta E_i[\text{MeV}]\left(\frac{\mu_{en}}{\rho}\right)_i \left[\frac{\text{cm}^2}{\text{g}}\right] \quad (1)$$

where Φ_i is the fluence per particle per MeV per cm^2 of the ith energy bin, E_i and is the energy of a photon within the ith energy bin, ΔE_i is the ith energy bin width, and $\left(\frac{\mu_{en}}{\rho}\right)_i$ is the mass energy absorption coefficient of the ith energy bin from NIST. This value is then converted to the air kerma rate in Gy/s with the unit conversion

$$K\left[\frac{\text{Gy}}{\text{s}}\right] = K\left[\frac{\text{MeV}}{\text{g particle}}\right] \times \frac{1.602\times10^{-13}\ \text{J}}{\text{MeV}} \times \frac{1000\ \text{g}}{\text{kg}} \times \frac{\text{particle}}{1.602\times10^{-19}\ \text{C}} \times I\left[\frac{\text{C}}{\text{s}}\right] \quad (2)$$

Table 2
Quantitative comparison of HVL1 and HVL2 between experimental measurements, MC simulated results, and SpekPy calculated values using copper attenuation. Results are given for beam energies of 200 kV, 160 kV, and 119 kV with a 0.25 mm Cu filter.

		HVL1 [mm]			HVL2 [mm]		
Material	Beam energy [kV]	MC	Experiment	SpekPy	MC	Experiment	SpekPy
Cu	200	0.77	0.74	0.71	2.26	2.24	2.10
Cu	160	0.57	0.56	0.54	1.58	1.60	1.50
Cu	119	0.38	0.36	0.36	0.97	1.00	0.97
Al	200	10.38	10.25	10.06	23.57	23.20	22.25
Al	160	8.92	9.25	8.82	20.50	19.57	19.62
Al	119	7.73	7.29	7.26	17.12	17.00	16.23

where I is the beam current setting used in the experimental setup.

To estimate the dose rate to water from air kerma rate, the dose to water ratio must be determined. To get this ratio, the fluence spectrum is first normalized to create an energy probability distribution for a given photon. The probability associated with each energy bin is multiplied by the interpolated mass energy absorption coefficient (MAC) from NIST for that energy value. These values are then summed using air and water MAC values separately over the entire energy range to calculate the dose to water ratio. This ratio is then multiplied by the air kerma rate to find the dose rate to water

$$D_W = K \frac{\left(\frac{\mu_{en}}{\rho}\right)_W}{\left(\frac{\mu_{en}}{\rho}\right)_{air}}. \tag{3}$$

It should be noted that while the EGSnrc software package supports direct calculation of dose to water using a specific module, this calculation does not include the full effects of scattered radiation from the irradiator geometry.

In this study, D_W represents the dose rate to water (Gy/s), corresponding to the energy deposited per unit mass of water per unit time. The conversion from the MC-calculated dose per particle to the physical dose rate is achieved through the beam current I (in C/s), which defines the number of incident particles per second and thereby introduces the time component of the dose rate. The water dose rate was obtained according to Eq. (3):

$$D_W = C\, I \sum_i \Phi_i\, E_i\, \Delta E_i \left(\frac{\mu_{en}}{\rho}\right)_i^{water} \frac{\left(\frac{\mu_{en}}{\rho}\right)_W}{\left(\frac{\mu_{en}}{\rho}\right)_{air}}, \tag{4}$$

where the conversion factor $C = 1.602\times10^{-13}/1.602\times10^{-19}\times1000 = 10^9$ ensures that the result is expressed in Gy/s.

The variance of D_W was propagated from the fluence variances through standard linear error-propagation analysis, assuming that the energy bins are statistically independent:

$$\sigma^2_{D_W} = \left(C\, I \frac{\left(\frac{\mu_{en}}{\rho}\right)_W}{\left(\frac{\mu_{en}}{\rho}\right)_{air}}\right)^2 \sum_i \left[E_i\, \Delta E_i \left(\frac{\mu_{en}}{\rho}\right)_i^{water} \sigma_{\Phi_i}\right]^2. \tag{5}$$

Here, σ_{Φ_i} is the standard deviation of the photon fluence in each energy bin, as reported by BEAMDP (the third column in the "@TYPE xydy" file); thus, $\sigma^2_{\Phi_i}$ enters the variance sum above. The square root of the propagated variance gives the standard deviation of D_W, i.e., $\sigma_{D_W} = \sqrt{\sigma^2_{D_W}}$, which represents the Monte Carlo component of the total uncertainty. Systematic uncertainties arising from the mass energy-absorption coefficients, beam-current calibration, and geometric setup were evaluated separately and are not included in this Monte Carlo variance propagation. The results of D_W and its associated standard deviation are summarized in Tables 4 and 5.

3. Results

3.1. Assessment of half-value layer beam quality

Fig. 5 shows example attenuation curves for copper and aluminum at 200 kV and 119 kV respectively, demonstrating an exponential decrease in dose as the thickness of the attenuator increased. Using copper, the beam is attenuated much faster than with aluminum, as expected. Tables 2 and 3 present a comparison of the simulated HVL values of BEAMnrc with the experimentally measured values and the predicted values of SpekPy. The simulated HVL of BEAMnrc matches very well with the experimental values, the absolute percentage difference generally staying near 5% or lower for both HVL1 and HVL2. The SpekPy Interpolate method shows lesser agreement with BEAMnrc, with HVL1 and HVL2 differences close to 5% to 6% for Al and occasionally reaching 8% to 9% for Cu. Beam quality measurements and simulations were performed using a 0.25 mm Cu filter.

3.2. Assessment of dose rate

3.2.1. Film measurements at different kV energies

We perform film dosimetry measurements for a filtered beam at 200 kV, 160 kV, and 119 kV using 0.5 mm Cu filtration. The measured dose rates, as shown in Table 4, range from 0.015 to 0.12 Gy/s for 200 kV, 0.0112 to 0.0.89 Gy/s for 160 kV, and 0.0069 to 0.055 Gy/s for 119 kV, depending on SSD. The error of measurement (EoM) is approximately 9% for the film measurements. This EoM is higher than the 2%–3% from the ion chamber, due the intrinsically higher uncertainty of radiochromic films as well as increased sensitivity to environmental conditions.

3.2.2. Ion chamber measurements at different kV energies

Ionization chamber measurements are also performed using the Markus ionization chamber for a filtered beam at 200 kV, 160 kV, and 119 kV using 0.5 mm Cu filtration. The measured dose rates, as shown in Table 5, range from 0.0165 to 0.132 Gy/s for 200 kV, 0.0118 to 0.092 Gy/s for 160 kV, and 0.0079 to 0.062 Gy/s for 119 kV, depending on SSD. The EoM is approximately 2%–3% across all SSD and beam energy values, indicating high reliability.

3.2.3. Monte Carlo simulation

We perform detailed BEAMnrc simulations for an orthovoltage X-ray tube operating at 119 kV, 160 kV, and 200 kV using 0.5 mm Cu filtration. The tube is modeled with a tungsten target and appropriate filtration to match the experimental conditions described previously. Fluence spectra are computed at SSD equal to those used in the various experimental measurements. These spectra are then converted to air kerma, dose to water, and dose rate values as previously described. Simulated dose rates are compared to experimentally measured dose rates under equivalent conditions below.

3.3. Inverse-square relation

The dependence of dose rate on SSD was evaluated for different tube voltages, as demonstrated in Fig. 6 left. The findings reveal a substantial inverse-square dependence, with the fitted curves demonstrating a high degree of congruence with the theoretical model ($R^2 > 0.9997$). The corresponding log–log plots (Fig. 6 right) yielded slopes

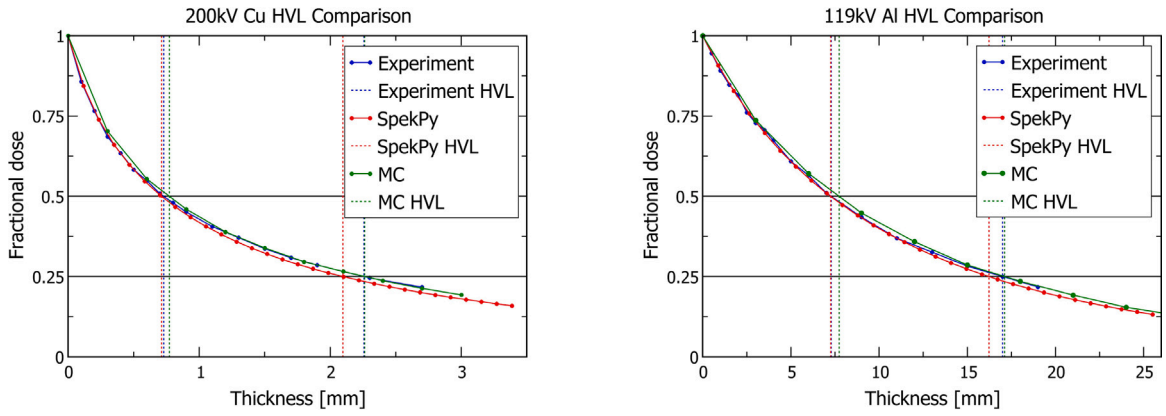

Fig. 5. Normalized attenuation curves with comparison of HVL1 and HVL2 between experimental measurements, MC simulated results, and SpekPy calculated values. Shown here are the attenuation curves for 200 kV with Cu attenuator plates (left) and 119 kV with Al attenuator plates (right).

Table 3
Quantitative comparison of HVL1 and HVL2 between experimental measurements, MC simulated results, and SpekPy calculated values using copper attenuation. Results are given for beam energies of 200 kV, 160 kV, and 119 kV with a 0.25 mm Cu filter. Absolute percent difference is given as the magnitude of the relative percent difference.

		HVL1 absolute percent difference		HVL2 absolute percent difference	
Material	Beam energy [kV]	MC vs. Experiment	MC vs. SpekPy	MC vs. Experiment	MC vs. SpekPy
Cu	200	4	9	1	8
Cu	160	2	6	1	5
Cu	119	6	6	1	4
Al	200	1	3	2	6
Al	160	4	1	5	5
Al	119	6	6	1	5

Table 4
Tables comparing measured dose rates using the EBT-XD radiochromic film to Monte Carlo simulated dose rates. Results are shown for 200 kV (top), 160 kV (middle), and 119 kV (bottom) with varying SSD. Absolute percent difference is given as the magnitude of the relative percent difference.

Film vs. MC dose rate (a) 200 kV			
SSD [cm]	Film [Gy/s]	MC [Gy/s]	Absolute percent difference
20.6	0.120 ± 0.009	0.117 ± 0.002	3
28.1	0.064 ± 0.005	0.064 ± 0.001	0
35.6	0.039 ± 0.003	0.040 ± 0.001	2
43.1	0.027 ± 0.002	0.0281 ± 0.0009	2
50.6	0.020 ± 0.001	0.021 ± 0.002	7
58.1	0.015 ± 0.001	0.0152 ± 0.0007	0
(b) 160 kV			
SSD [cm]	Film [Gy/s]	MC [Gy/s]	Absolute percent difference
20.6	0.089 ± 0.007	0.091 ± 0.003	3
28.1	0.047 ± 0.003	0.049 ± 0.001	5
35.6	0.029 ± 0.002	0.0286 ± 0.0008	2
43.1	0.020 ± 0.001	0.020 ± 0.001	0
50.6	0.015 ± 0.001	0.0144 ± 0.0006	4
58.1	0.0112 ± 0.0009	0.0114 ± 0.0006	2
(c) 119 kV			
SSD [cm]	Film [Gy/s]	MC [Gy/s]	Absolute percent difference
20.6	0.055 ± 0.005	0.055 ± 0.002	0
28.1	0.028 ± 0.002	0.028 ± 0.001	2
35.6	0.018 ± 0.002	0.0183 ± 0.0009	2
43.1	0.011 ± 0.001	0.0110 ± 0.0006	11
50.6	0.0091 ± 0.0008	0.0093 ± 0.0008	2
58.1	0.0069 ± 0.0007	0.0072 ± 0.0005	5

Table 5
Tables comparing measured dose rates using the Markus ionization chamber to Monte Carlo simulated dose rates. Results are shown for 200 kV (top), 160 kV (middle), and 119 kV (bottom) with varying SSD. Absolute percent difference is given as the magnitude of the relative percent difference.

Markus vs. MC dose rate (a) 200 kV			
SSD [cm]	Markus [Gy/s]	MC [Gy/s]	Absolute percent difference
20.1	0.132 ± 0.003	0.130 ± 0.002	1
27.6	0.069 ± 0.001	0.070 ± 0.001	2
35.1	0.0426 ± 0.0009	0.0436 ± 0.0009	2
42.6	0.0295 ± 0.0006	0.0300 ± 0.0008	2
50.1	0.0215 ± 0.0004	0.0214 ± 0.0008	0
57.6	0.0165 ± 0.0003	0.0165 ± 0.0006	0
(b) 160 kV			
SSD [cm]	Markus [Gy/s]	MC [Gy/s]	Absolute percent difference
20.1	0.092 ± 0.002	0.098 ± 0.002	7
27.6	0.049 ± 0.001	0.052 ± 0.001	7
35.1	0.0303 ± 0.0006	0.0325 ± 0.0007	7
42.6	0.0210 ± 0.0004	0.0217 ± 0.0008	5
50.1	0.0153 ± 0.0003	0.0159 ± 0.0008	4
57.6	0.0118 ± 0.0002	0.0123 ± 0.0006	5
(c) 119 kV			
SSD [cm]	Markus [Gy/s]	MC [Gy/s]	Absolute percent difference
20.1	0.062 ± 0.001	0.062 ± 0.002	0
27.6	0.0332 ± 0.0007	0.032 ± 0.001	3
35.1	0.0207 ± 0.0004	0.0195 ± 0.0007	5
42.6	0.0143 ± 0.0003	0.0133 ± 0.0007	7
50.1	0.0104 ± 0.0002	0.0099 ± 0.0007	5
57.6	0.0079 ± 0.0002	0.0076 ± 0.0005	3

ranging from −1.991 to −1.996, with uncertainties below 2%, thus confirming the validity of the inverse-square relationship. Although slight deviations from the inverse-square law are often expected in open geometries due to increased scatter and beam divergence, the strong agreement observed here is likely related to the specific experimental configuration. The Markus ionization chamber was positioned inside a water equivalent phantom (water–chamber–water configuration), which helped to maintain consistent scatter conditions and

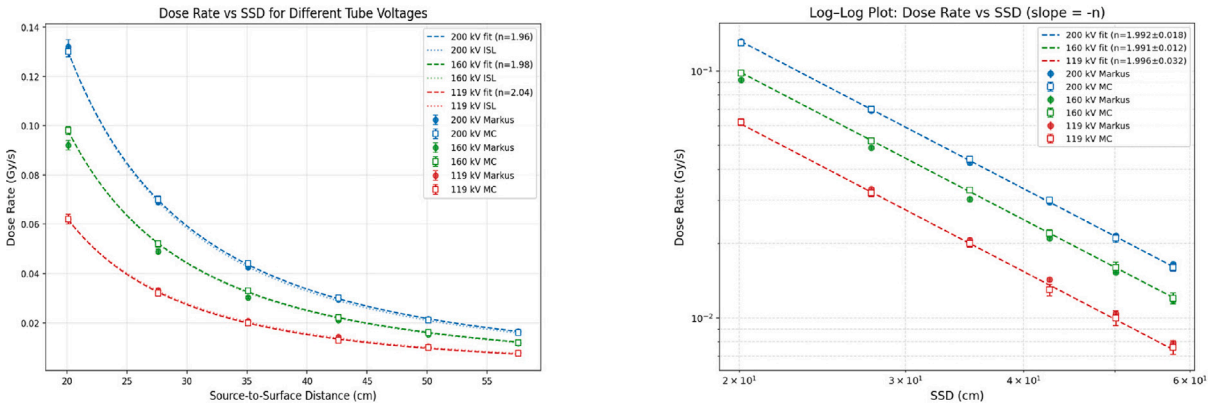

Fig. 6. Left: Measured dose rate as a function of SSD for various tube voltages. Monte Carlo data was fitted to a power law ($D = a \times \mathrm{SSD}^{-n}$) (dashed lines) and to the ideal inverse-square law ($n = 2$) (dotted line). Right: Log–log plot of dose rate versus SSD for a range of tube voltages. Linear fits (dashed lines) were applied to the data, and the slope values close to −2 confirm the inverse-square dependence.

Table 6
Quantitative comparison of HVL1 and HVL2 between experimental measurements and SpekPy calculated values with copper and aluminum attenuation. Results are given for beam energies of 200 kV, 160 kV, and 119 kV. Absolute percent difference is given as the magnitude of the relative percent difference.

SpekPy HVL
(a) HVL comparison

	HVL1 [mm]			HVL2 [mm]		
Beam energy [kV]/ attenuator material	Experiment	SpekPy interpolate	SpekPy function	Experiment	SpekPy interpolate	SpekPy function
200 Cu	0.74	0.71	0.69	1.36	1.38	1.34
160 Cu	0.56	0.54	0.52	0.94	0.96	0.93
119 Cu	0.36	0.36	0.36	0.60	0.60	0.59
200 Al	10.25	10.06	9.88	12.00	12.19	12.04
160 Al	9.25	8.82	8.68	10.37	10.80	10.67
119 Al	7.29	7.26	7.15	8.95	8.97	8.87

(b) SpekPy absolute percent difference in HVL values

	Absolute percent difference in HVL1		Absolute percent difference in HVL2	
Beam energy [kV]/ attenuator material	Experiment vs. SpekPy interpolate	Experiment vs. SpekPy function	Experiment vs. SpekPy interpolate	Experiment vs. SpekPy function
200 Cu	4	7	2	1
160 Cu	4	8	3	0
119 Cu	0	2	0	3
200 Al	2	4	2	0
160 Al	5	6	4	3
119 Al	0	2	0	1

minimize variations due to air gaps. This geometry effectively preserved near-ideal point-source conditions, leading to a dose fall-off that closely followed the inverse-square law across all tested SSDs.

4. Discussion

4.1. Assessment of half-value layer for beam quality

The attenuation curves confirm the expected exponential reduction in dose as X-ray beams pass through increasingly thick copper and aluminum attenuators. Higher voltages demonstrate reduced attenuation rates, consistent with deeper penetration due to higher energy spectra. The BEAMnrc simulation accurately predicts both HVL1 and HVL2 values, validating its effectiveness for simulating experimental conditions. The small discrepancies observed could be attributed to beam hardening effects, differences in the spectral modeling of the X-ray beam, and effects from the geometry. The greater discrepancy with SpekPy is expected since SpekPy does not include the same degree of complexity and rigor used in MC simulations, such as accounting for scattering effects. Further investigation is required to enhance the accuracy of SpekPy HVL predictions, particularly for high-energy configurations.

4.2. Assessment of dose rate

It is shown that there is close agreement between experimentally measured and MC simulated dose rate values. This remains consistent across a wide range of SSD values (20.1 to 57.6 cm for Markus and 20.6 to 58.1 cm for films) and beam energies (200, 160, and 119 kV). Simulated values generally fall within EoM ranges for experimentally measured dose rates.

At 200 kV, the percent difference between the measured dose rate using the Markus ionization chamber and MC simulation ranges from 0 to 2%. For films at this energy level, the percent differences range from 0 to 7%, with most values being 3% or less. For 160 kV, the percent difference between the measured dose rate using the Markus ionization chamber and MC simulation ranges from 3 to 7%. For films, the percent differences range from 2 to 5%. Finally, for 119 kV, the percent difference between the measured dose rate using the Markus ionization chamber and MC simulation ranges from 0 to 7%, with most of the values being 5% or less. For films, the percent difference ranges from 0 to 11%, with most values again being 2% or less and 11% as an outlier.

The change in percent difference with respect to beam energy and SSD is minor and we do not observe any trend or dependency on

either. Thus, the simulation accuracy is independent of beam energy and SSD. Additionally, we do not observe significant differences in the percent difference comparing the MC simulation to films or the ionization chamber.

The approximate 9% uncertainty observed in this study can be attributed to several factors. The response exhibited by Gafchromic EBT-XD films demonstrates a weak yet significant correlation with photon energy within the orthovoltage range [31]. Furthermore, this uncertainty is partly attributable to the calibration curve fitting residuals, particularly in the low-dose region where the film response deviates from linearity [35]. The combined effects of these factors contribute to the comparatively higher uncertainty observed in this study.

5. Conclusion

We perform a rigorous dosimetric study for the MultiRad225 X-ray irradiator using a combination of experimental and simulation techniques for both beam quantity and quality. The simulation model uses a comprehensive geometry which accurately portrays the experimental irradiator. Because of this, the simulation is able to fully account for any scattering effects from the surrounding materials.

For experimental dosimetry, radiochromic films and an ionization chamber are used. Both of these are explicitly modeled within the simulations as well. The results and comparisons are made at beam energies of 119, 160, and 200 kV, and SSD values ranging from 20.1 to 58.1 cm. We obtain a close overall agreement between experimentally measured results for both beam quantity and beam quality measurements. The simulated values fall within the expected experimental uncertainty range for the measurements, indicating a good overall quality of our model.

CRediT authorship contribution statement

E. Theodoridou: Conceptualization, Methodology, Validation, Formal analysis, Investigation, Data curation, Writing – original draft, Writing – review & editing, Visualization, Supervision, Project administration. **R. Dong:** Conceptualization, Methodology, Software, Validation, Formal analysis, Investigation, Resources, Writing – original draft, Writing – review & editing, Visualization, Project administration. **C.C. King:** Conceptualization, Methodology, Software, Validation, Formal analysis, Investigation, Data curation, Writing – original draft, Writing – review & editing, Visualization, Supervision, Project administration. **G. Poludniowski:** Methodology, Software, Writing – review & editing, Supervision. **P. Häring:** Methodology, Writing – review & editing, Supervision. **E. Hain:** Validation, Investigation. **C. Litou:** Validation, Investigation. **E. Voutou:** Validation, Investigation. **P. Foka:** Writing – review & editing, Supervision. **N. Sammut:** Writing – review & editing, Supervision. **J. Seco:** Conceptualization, Methodology, Resources, Writing – review & editing, Supervision, Project administration, Funding acquisition. **M.F. Spadea:** Writing – review & editing, Supervision, Funding acquisition.

Declaration of competing interest

The authors declare that they have no known competing financial interests or personal relationships that could have appeared to influence the work reported in this paper.

Appendix. SpekPy HVL

As detailed in the SpekPy software documentation [25], SpekPy supports direct calculation of the first and second HVL values. While this is the easiest and most straightforward method of calculating HVL, we observe minor discrepancies using this SpekPy function. These discrepancies are most prominent with HVL1. Because of this, we develop the interpolation approach explained previously. Table 6 shows our comparison between experimentally derived HVL values and the two SpekPy methods.

It is seen that although the HVL1 difference between experiment and the SpekPy function is small, the interpolate method still gives better agreement across all energy and attenuator material combinations. With HVL2, both methods perform equally well. Due to the better agreement with the experimentally measured HVL1, we use the interpolation method for our HVL calculations.

References

[1] Miller K, Nogueira L, Mariotto A, Rowland J, Yabroff K, Alfano C, Jemal A, Kramer J, Siegel R. Cancer treatment and survivorship statistics, 2019. CA: Cancer J Clin 2019;69(5):363–85. http://dx.doi.org/10.3322/caac.21565, URL https://acsjournals.onlinelibrary.wiley.com/doi/10.3322/caac.21565.

[2] Geirnaert F, Kerkhove L, Montay-Gruel P, Gevaert T, Dufait I, De Ridder M. Exploring the metabolic impact of FLASH radiotherapy. Cancers 2025;17(1):133. http://dx.doi.org/10.3390/cancers17010133, URL https://www.mdpi.com/2072-6694/17/1/133.

[3] Mizoe J-E, Tsujii H, Hasegawa A, Yanagi T, Takagi R, Kamada T, Tsuji H, Takakura K, of the Central Nervous System Tumor Working Group OC, et al. Phase I/II clinical trial of carbon ion radiotherapy for malignant gliomas: combined X-ray radiotherapy, chemotherapy, and carbon-ion radiotherapy. Int J Radiat Oncol* Biol* Phys 2007;69(2):390–6. http://dx.doi.org/10.1016/j.ijrobp.2007.03.003.

[4] Burnet NG, Mee T, Gaito S, Kirkby NF, Aitkenhead AH, Anandadas CN, Aznar MC, Barraclough LH, Borst G, Charlwood FC, Clarke M, Colaco RJ, Crellin AM, Defourney NN, Hague CJ, Harris M, Henthorn NT, Hopkins KI, Hwang E, Ingram SP, Kirkby KJ, Lee LW, Lines D, Lingard Z, Lowe M, Mackay RI, McBain CA, Merchant MJ, Noble DJ, Pan S, Price JM, Radhakrishna G, Reboredo-Gil D, Salem A, Sashidharan S, Sitch P, Smith E, Smith EAK, Taylor MJ, Thomson DJ, Thorp NJ, Underwood TSA, Warmenhoven JW, Wylie JP, Whitfield G. Estimating the percentage of patients who might benefit from proton beam therapy instead of X-ray radiotherapy. Br J Radiol 2022;95(1133):20211175. http://dx.doi.org/10.1259/bjr.20211175.

[5] Goitein M, Jermann M. The relative costs of proton and X-ray radiation therapy. Clin Oncol 2003;15(1):S37–50. http://dx.doi.org/10.1053/clon.2002.0174.

[6] Kubo N, Saitoh J-i, Shimada H, Shirai K, Kawamura H, Ohno T, Nakano T. Dosimetric comparison of carbon ion and X-ray radiotherapy for stage IIIA non-small cell lung cancer. J Radiat Res 2016;57(5):548–54. http://dx.doi.org/10.1093/jrr/rrw041.

[7] Bartzsch S, Cordé S, Crosbie JC, Day L, Donzelli M, Krisch M, Lerch M, Pellicioli P, Smyth LML, Tehei M. Technical advances in x-ray microbeam radiation therapy. Phys Med Biol 2020;65(2):02TR01. http://dx.doi.org/10.1088/1361-6560/ab5507.

[8] Jung S, Sung W, Lee J, Ye SJ. MCNP6.1 simulations for low-energy atomic relaxation: Code-to-code comparison with GATEv7.2, PENELOPE2014, and EGSnrc. Nucl Instrum Methods Phys Res Sect B 2018;432:56–60. http://dx.doi.org/10.1016/j.nimb.2017.11.024, URL https://www.sciencedirect.com/science/article/abs/pii/S0168583X17309874.

[9] Chatzisavvas N, Koustas T, Karpetas G, Valais I, Priniotakis G, Nikolopoulos D. Simulating medical imaging X-Ray tubes with various parameters using beamnrc Monte Carlo software. Open J Radiol 2022;12:125–41. http://dx.doi.org/10.4236/ojrad.2022.123014, URL https://www.scirp.org/journal/paperinformation?paperid=120112.

[10] Watson PGF, Seuntjens J. Technical note: Effect of explicit M and N-shell atomic transitions on a low-energy x-ray source. Med Phys 2016;43(4):1760–3. http://dx.doi.org/10.1118/1.4943954, URL https://aapm.onlinelibrary.wiley.com/doi/10.1118/1.4943954.

[11] Precision X-Ray, Inc. MultiRad 225 X-ray Irradiation System. 2025, https://precisionxray.com/system/multirad225/. (Accessed 22 October 2025).

[12] He Y, Peng Y, Chang Y, Zhu J, Li Z, Huang K, Pan S. Utilizing the faxitron MultiRad 225 X-ray irradiation system for the construction of mouse chronic whole brain radiation model. J Radiat Res 2021;62(6):966–75. http://dx.doi.org/10.1093/jrr/rrab086.

[13] Saikkonen A, Niemelä J, Sipilä P, Keyriläinen J. Commissioning of the MultiRad 350 cell and small animal x-ray irradiation system. Phys Medica 2019;59:107–11. http://dx.doi.org/10.1016/j.ejmp.2019.03.004.

[14] Torres Filho IP, Torres LN, Barraza D, Williams CE, Hildreth K. Cellular and biochemical effects of combined X-Ray radiation and storage on whole blood. Dose-Response 2022;20(1):15593258211073100. http://dx.doi.org/10.1177/15593258211073100.

[15] Stengl C, Arbes E, Thai L-YJ, Echner G, Vedelago J, Jansen J, Jäkel O, Seco J. Development and characterization of a versatile mini-beam collimator for preclinical photon beam irradiation. Med Phys 2023;50(8):5222–37. http://dx.doi.org/10.1002/mp.16432.

[16] Lechner M, Kolz A, Herre K, Matzek D, Schomburg A, Popper B. Custom-made 3D-printed X-ray shield for tumor-specific irradiation of xenograft mice, 11 (1) (2025) 17. http://dx.doi.org/10.1186/s41205-025-00264-z.

[17] Healy BJ, Hill RF. Use of calculations to validate beam quality and relative dose measurements for a kilovoltage X-ray therapy unit. Phys Eng Sci Med 2022;45(2):537–46. http://dx.doi.org/10.1007/s13246-022-01120-8, URL https://link.springer.com/article/10.1007/s13246-022-01120-8.

[18] Reynoso F, Cho S. SU-E-T-557: Monte Carlo modeling of philips RT-250 orthovoltage unit for beam spectrum modulation. Med Phys 2015;42(6):3586. http://dx.doi.org/10.1118/1.4924919, URL https://www.osti.gov/biblio/22496272.

[19] Iseri T, Tanabe Y, Onizuka R, Torigoe Y, Horikirizono H, Itamoto K, Sunahara H, Itoh H, Tani K, Nakaichi M. A Monte Carlo study on dose distribution of an orthovoltage radiation therapy system. Phys Eng Sci Med 2023;46(2):623–32. http://dx.doi.org/10.1007/s13246-023-01237-4, URL https://link.springer.com/article/10.1007/s13246-023-01237-4.

[20] Pottage T, Garratt I, Birch C, Parks S, Bennett A. X-ray inactivation of RNA viruses without loss of biological characteristics. Sci Rep 2020;10(1):20421. http://dx.doi.org/10.1038/s41598-020-77972-5, URL https://www.nature.com/articles/s41598-020-77972-5.

[21] Pottage T, Garratt I, Birch C, Bennett A, Parks S. Monte Carlo modelling of an x-ray chamber for providing inactivation exposures to viruses. J Radiol Prot 2021;41(4):S645–60. http://dx.doi.org/10.1088/1361-6498/ac2f85, URL https://pubmed.ncbi.nlm.nih.gov/34644683/.

[22] Bazalova-Carter M, Esplen N. On the capabilities of conventional x-ray tubes to deliver ultra-high (FLASH) dose rates. Med Phys 2019;46(12):5690–5. http://dx.doi.org/10.1002/mp.13858, URL https://aapm.onlinelibrary.wiley.com/doi/10.1002/mp.13858.

[23] PTW Freiburg GmbH. Detectors for ionizing radiation: Online catalogue. 2025, https://www.ptwdosimetry.com/fileadmin/user_upload/Online_Catalog/Detectors_for_Ionizing_Radiation/index.html?startpage=1.

[24] Kawrakow I, Rogers DWO, Mainegra-Hing E, Tessier F, Townson RW, Walters BRB. EGSnrc toolkit for Monte Carlo simulation of ionizing radiation transport. 2000, http://dx.doi.org/10.4224/40001303, URL https://nrc-cnrc.github.io/EGSnrc/. software toolkit, EGSnrc software.

[25] Poludniowski G, Vorbau R. Spekpy: A python toolkit for modeling X-ray tube spectra. 2024, https://bitbucket.org/spekpy/spekpy_release/wiki/Home. (Accessed 23 August 2024).

[26] Omar A, Andreo P, Poludniowski G. A model for the energy and angular distribution of x rays emitted from an x-ray tube. Part I. Bremsstrahlung production. Med Phys 2020;47(10):4763–74. http://dx.doi.org/10.1002/mp.14359, URL https://aapm.onlinelibrary.wiley.com/doi/10.1002/mp.14359.

[27] Omar A, Andreo P, Poludniowski G. A model for the energy and angular distribution of x rays emitted from an x-ray tube. Part II. Validation of x-ray spectra from 20 to 300 kV. Med Phys 2020;47(9):4005–19. http://dx.doi.org/10.1002/mp.14360, URL https://aapm.onlinelibrary.wiley.com/doi/10.1002/mp.14360.

[28] International Atomic Energy Agency. Absorbed dose determination in external beam radiotherapy: An international code of practice for dosimetry based on standards of absorbed dose to water (TRS-398). Vienna, Austria: International Atomic Energy Agency; 2024, URL https://www.iaea.org/publications/5954/absorbed-dose-determination-in-external-beam-radiotherapy. (Accessed 2024).

[29] Devic S, Tomic N, Lewis D. Reference radiochromic film dosimetry: Review of technical aspects. Phys Medica 2016;32(4):541–56. http://dx.doi.org/10.1016/j.ejmp.2016.02.008, URL https://www.physicamedica.com/article/S1120-1797(16)00510-X/abstract.

[30] Massillon-JL G, Chiu-Tsao S-T, Domingo-Munoz I, Chan MF. Energy dependence of the new gafchromic EBT3 film: dose response curves for 50 kV, 6 and 15 MV X-ray beams. Int J Med Phys Clin Eng Radiat Oncol 2012;1(2). http://dx.doi.org/10.4236/ijmpcero.2012.12008.

[31] Ashland Inc. Gafchromic™ EBT-XD film — Performance data & practical user guidelines. Technical report pha21-011, Ashland Inc.; 2021, URL https://www.ashland.com/file_source/Ashland/Documents/PHA21-011_Gafchromic%20EBT-XD%20Protocol.pdf. (Accessed 24 October 2025).

[32] Araki F. Determination of an ionization chamber response using quality index for kilovoltage x-ray beams. Radiat Phys Chem 2021;188:109595. http://dx.doi.org/10.1016/j.radphyschem.2021.109595.

[33] Healy B, Gibbs A, Murry R, Prunster J, Nitschke K. Output factor measurements for a kilovoltage X-ray therapy unit. Australas Phys Eng Sci Med 2005;28(2):115–21. http://dx.doi.org/10.1007/BF03178702.

[34] Darafsheh A. On energy dependency, spectral properties, and orientation dependency of EBT3, EBT-XD, MD-v3, and HD-V2 radiochromic films. Phys Med Biol 2025;70(8):085015. http://dx.doi.org/10.1088/1361-6560/adcafc.

[35] Lewis D, Micke A, Yu X, Chan MF. An efficient protocol for radiochromic film dosimetry combining calibration and measurement in a single scan. Med Phys 2012;39(10):6339–50. http://dx.doi.org/10.1118/1.4754797.